High precision metrology based microwave effective linewidth measurement technique

Nan Mo, Jerome J. Green, Bailey A. Beitscher, and Carl E. Patton
Department of Physics, Colorado State University, Fort Collins, Colorado 80523, USA

(Received 7 September 2007; accepted 17 October 2007; published online 19 November 2007)

A precision microwave effective linewidth measurement technique for magnetic samples has been developed. The measurement utilizes a high-Q cylindrical cavity that contains the sample of interest, a highly stable and programable static magnetic field source, a computer controlled network analyzer for cavity center frequency ω_c and quality factor Q_c determinations, and the standard metrological substitution *ABA* method for accurate relative ω_c and Q_c measurements. Sequential long term *ABA* measurements show that the time and temperature drifts and random errors are the dominant sources of error, with uncertainties in $\omega_c/2\pi$ and Q_c in the range of 50 kHz and 25, respectively. The *ABA* method is applied to eliminate these drifts and minimize the random errors. For measurements over 25 *ABA* cycles, accuracy is improved to 0.14 kHz for $\omega_c/2\pi$ and 3 for Q_c. The temperature variation over a single *ABA* cycle is generally on the order of $10^{-3}-10^{-5}$ °C and there is no need for any further temperature stabilization or correction measures. The overall uncertainty in the 10 GHz effective linewidth determinations for a 3 mm diam, 0.5 mm thick polycrystalline yttrium iron garnet (YIG) disk is 0.15 Oe or less, well below the intrinsic single crystal YIG linewidth. This represents a factor of 10 improvement in measurement accuracy over previous work. © *2007 American Institute of Physics.* [DOI: 10.1063/1.2813344]

I. INTRODUCTION

The effective linewidth approach to microwave loss in magnetic materials has proven to be useful for both the fundamental understanding of relaxation processes and the prediction of device performance. The technique was first developed by Kohane and Schlömann[1] in 1968 for loss determinations in the high field regime, well above the ferromagnetic resonance (FMR) field for a fixed frequency. Further work in the near FMR, high field, and low field regimes[2–25] has established the method as a valid way to obtain on-, near-, and off-resonance microwave loss parameters versus field for a wide range of ferrite and metallic thin film systems.

The approach is based on the fact that for systems in which two magnon scattering processes contribute significantly to the microwave loss, the relaxation rate η for the driven dynamic mode in a microwave experiment is magnetic field (H) dependent. For magnetically saturated spheres, the FMR linewidth ΔH_{FMR} is equal to $2\eta(H_{\mathrm{FMR}})/|\gamma(H_{\mathrm{FMR}})|$, where H_{FMR} is the FMR field and γ denotes the effective gyromagnetic ratio, which may also be field dependent. It proves convenient to define the field dependent effective linewidth, $\Delta H_{\mathrm{eff}}(H)=2\eta(H)/|\gamma(H)|$. This ΔH_{eff} parameter simply expresses the field dependent relaxation rate in convenient linewidth units. Gaussian units are used here and below.

The effective linewidth determination is based on measurements of the complex susceptibility $\chi_e=\chi_e'-i\chi_e''$ vs H for the sample and the experimental geometry of interest. Unlike the usual FMR linewidth, the ΔH_{eff} parameter cannot be determined exclusively from the power absorption or $\chi_e''(H)$ response. Rather, one has to measure both the real part $\chi_e'(H)$ and negative imaginary part $\chi_e''(H)$ of the susceptibility. These susceptibility components can be written as a function of $\eta(H)$ and $\gamma(H)$ based on the magnetic torque equation and a suitable damping model. For most of the work cited above, a simple complex frequency damping model was used. The $\eta(H)$ and $\gamma(H)$ parameters as well as the derived ΔH_{eff} as defined above may be evaluated analytically or numerically from the working susceptibility equations and the data.

Microwave cavity techniques for the measurement of the complex microwave susceptibility are well developed and time tested.[26–30] The sample of interest is generally mounted inside a microwave cavity. One first obtains the cavity center frequency $\omega_c(H)$ and quality factor $Q_c(H)$ for all fields of interest. One then applies microwave cavity perturbation theory[26] to extract $\chi_e'(H)$ and $\chi_e''(H)$ from these cavity data. The key experimental step for a full $\Delta H_{\mathrm{eff}}(H)$ determination is in the accurate measurement of $\omega_c(H)$ and $Q_c(H)$ for a suitably loaded cavity and the desired range of fields.

The accurate measurement of $\omega_c(H)$ and $Q_c(H)$ over the full range of field values of interest is not a simple matter. This is because the $\chi_e'(H)$ and especially the $\chi_e''(H)$ values can be very small when the sample is biased far from the FMR field. As an example, while χ_e'' at the FMR field can be on the order of 100 for a polycrystalline yttrium iron garnet (YIG) sphere, it can be on the order of 10^{-5} or less far from resonance. In order to obtain meaningful effective linewidth results, a high accuracy susceptibility measurement is extremely important. This exacerbates the need for high accuracy $\omega_c(H)$ and $Q_c(H)$ measurements.

The importance of very high cavity measurement accuracy for effective linewidth determinations has been realized

 © 2007 American Institute of Physics

Downloaded 28 Nov 2007 to 129.82.140.121. Redistribution subject to AIP license or copyright; see http://rsi.aip.org/rsi/copyright.jsp

since the 1970's. In 1972, Patton and Kohane[27] developed and reported on a high sensitivity susceptibility measurement technique based on the use of high Q cavity in a transmission cavity microwave spectrometer. Accurate measurements down to about 10^{-4} in χ_e' and 10^{-5} in χ_e'' were demonstrated for YIG spheres. Since the 1990's, modern synthesized sweep oscillator and network analyzer methods have generally replaced the old technology.[16] Up to now, however, such advances have not had a significant impact on the measurement sensitivity in the regime of low χ_e.

As discussed by Hoeppe,[31] high accuracy microwave susceptibility measurements involve more than sensitivity considerations. There are three main error sources to be considered: drifts, imperfect cavity temperature stabilization, and random errors. It will be shown in Sec. IV that these errors can be significant, especially for microwave susceptibility measurements at high and low fields.

Three measures are given in this paper for the improvement of cavity measurement accuracy for precision effective linewidth determinations. First, the effective linewidth spectrometer system is optimized to reduce the systematic distortions due to imperfections and mismatches of the system components and improve the stability of measurement system. Second, the time and temperature drifts are eliminated through the use of metrological substitution methods.[33,34] Finally, the random errors are minimized by averaging over many measurements.

The technique developed below is applicable to samples with a general shape and at any field. For convenience and consistency, this paper will focus on high field effective (HFE) linewidth measurements for in-plane magnetized polycrystalline YIG disks driven by an in-plane linearly polarized microwave magnetic field perpendicular to the static field. The paper is organized as follows. Section II reviews the overall effective linewidth measurement method. Section III gives a description of the spectrometer system. The improvements in system stability are also discussed in this section. Section IV summarizes the work needed to identify the dominant error sources and the nature of these errors. Section V introduces the metrological substitution *ABA* method for the elimination or minimization of the dominant errors. Section VI presents example results from the full effective linewidth measurement procedure. Section VII gives a summary and conclusions.

II. EFFECTIVE LINEWIDTH MEASUREMENT METHOD: WORKING EQUATIONS

One starts with the standard small signal microwave response of an in-plane magnetized ferrite disk defined through the complex external susceptibility tensor χ_e. In the experiment, the cavity is used to measure the diagonal component χ_{eh} of this tensor that corresponds to the direction of the microwave field **h**. One can easily show that the power absorbed by a ferrite sample scales with the negative imaginary part of this susceptibility component, here taken as χ_{eh}'', that corresponds to the direction of the transverse microwave field at the sample position. The full width at half maximum of the χ_{eh}'' versus field loss profile corresponds to the usual FMR linewidth ΔH_{FMR}.

One may obtain relatively simple expressions for the complex χ_{eh} component from a torque equation of motion analysis with microwave loss introduced through a complex frequency approach or some other means. For an in-plane magnetized YIG disk driven by a uniform linearly polarized in-plane microwave magnetic field perpendicular to the static field at a frequency ω_s and for a relatively high field that is many linewidths away from the FMR field, one may write the real and negative imaginary components of χ_{eh} as[22]

$$\chi_{eh}' = \frac{M_s H_\perp}{H_{\mathrm{FMR}}^2 - (\omega_s/\gamma)^2} \tag{1}$$

and

$$\chi_{eh}'' = \frac{1}{2}\frac{M_s[H_\perp^2 + (\omega_s/\gamma)^2]}{[H_{\mathrm{FMR}}^2 - (\omega_s/\gamma)^2]^2}\Delta H_{\mathrm{eff}}. \tag{2}$$

Here, M_s denotes the magnetization of the sample. The fields $H_\perp = H + 4\pi M_s(N_\perp - N_\parallel)$ and $H_\parallel = H$ represent effective stiffness fields, where $N_\perp$ and $N_\parallel$ are the demagnetizing factors along the out-of-plane and in-plane directions of the disk, respectively, and H_{FMR} is equal to $\sqrt{H_\perp H_\parallel}$. In the above, it is assumed that $\Delta H_{\mathrm{eff}} \ll |H - H_{\mathrm{FMR}}|$ is true. That is, the field operating point for the measurement is many linewidths away from the FMR field. Note that χ_{eh}' does not depend on the effective linewidth, only on known materials or experimental parameters, while χ_{eh}'' depends on these same parameters and also scales linearly with ΔH_{eff}. These forms are central to the high field effective linewidth analysis. One can also see that in the high field limit, χ_{eh}' and χ_{eh}'' fall off as $1/H$ and $1/H^2$, respectively.

The above expressions are based on uniform mode FMR theory. Experimentally, these χ_{eh}' and χ_{eh}'' parameters for a given field can be determined from measurements of the field dependent cavity center frequency $\omega_c(H)$ and quality factor $Q_c(H)$ for the microwave cavity containing the sample. From cavity perturbation theory,[26] the relevant connections for the present purposes may be written as

$$4\pi\chi_{eh}' = -K\frac{\omega_c - \omega_\infty}{\omega_c} \tag{3}$$

and

$$4\pi\chi_{eh}'' = \frac{K}{2}\left(\frac{1}{Q_c} - \frac{1}{Q_\infty}\right), \tag{4}$$

where ω_∞ and Q_∞ correspond to the frequency and quality factor of the cavity, respectively, at very high field with the magnetic effects frozen out. Here, the cavity center frequency ω_c is taken to be equal to ω_s. The K parameter is a cavity calibration factor that scales with the volume of the sample and depends on the nature of the electromagnetic mode and the sample position in the cavity. These parameters are generally obtained from a high field extrapolation procedure that will be discussed shortly. The connections in Eqs. (3) and (4) are valid as long as the cavity loading is relatively small and the corresponding changes in ω_c and Q_c, relative to ω_∞ and Q_∞, are not too large. Generally speaking, the form of Eqs. (3) and (4) is valid if these relative changes are on the order of 20% or less.

Downloaded 28 Nov 2007 to 129.82.140.121. Redistribution subject to AIP license or copyright; see http://rsi.aip.org/rsi/copyright.jsp

Because of the small but significant change in the cavity Q_c with frequency due to eddy current losses in the cavity walls, it is also important to apply a correction to Eq. (4). To the lowest order, the change in frequency due to the effect of $\chi'_{eh}(H)$ gives rise to a change in Q_c that may be written as[25]

$$\delta Q_c = Q_\infty(\omega_c - \omega_\infty)/2\omega_c. \tag{5}$$

One uses this δQ_c, as obtained directly from the data, to back correct the measured Q_c to the frequency corrected value. Because the effect is small, one can also take the expedient to replace the as yet undetermined ω_∞ parameter in Eq. (5) with the actual cavity frequency at the highest measurement field. Based on these procedures, the operational replacement equation for Eq. (4) is then given as

$$4\pi\chi''_{eh} = \frac{K}{2}\left(\frac{1}{Q_c - \delta Q_c} - \frac{1}{Q_\infty}\right) = \frac{K}{2}\frac{Q_\infty - Q_c + \delta Q_c}{(Q_c - \delta Q_c)Q_\infty}. \tag{6}$$

Prior to the susceptibility analysis to obtain $\Delta H_{\text{eff}}(H)$, calibrations are made for the determination of K, ω_∞, and Q_∞. This is done from a consideration of working high field equations based on Eqs. (1)–(3) and (6). One may rewrite Eqs. (3) and (6) as

$$\omega_c = -\frac{1}{K}X_\omega + \omega_\infty \tag{7}$$

and

$$\frac{1}{Q_c - \delta Q_c} = \frac{\Delta H_{\text{eff}}}{K}X_Q + \frac{1}{Q_\infty}, \tag{8}$$

respectively, where the X_ω and X_Q parameters follow directly from Eqs. (1) and (2) according to

$$X_\omega = \frac{4\pi M_s H_\perp \omega_c}{H_{\text{FMR}}^2 - (\omega_c/\gamma)^2} \tag{9}$$

and

$$X_Q = \frac{4\pi M_s[H_\perp^2 + (\omega_c/\gamma)^2]}{[H_{\text{FMR}}^2 - (\omega_c/\gamma)^2]^2}. \tag{10}$$

In the extreme high field limit, X_ω and X_Q tend to zero as $1/H$ and $1/H^2$, respectively. The ω_c vs X_ω response in the above-manifold field regime is expected to be highly linear. As evident from Eq. (7), a linear fit to high field data can then yield both ω_∞ and K. This is also the step in the analysis at which an empirical determination of the γ parameter is made. This is done by adjusting γ to optimize the accuracy of the linear fit to the ω_c vs X_ω response.[24] The details of the high field quality factor $Q_c - \delta Q_c$ vs X_Q response, however, depend on the relaxation mechanisms in play. References 22 and 24 demonstrate the specific cases of eddy current losses and electromagnetic spin wave scattering, respectively. A proper fit of the $Q_c - \delta Q_c$ vs X_Q response gives Q_∞. The reader is referred to Refs. 22 and 24 for details on the determination of K, ω_∞, and Q_∞.

The $\Delta H_{\text{eff}}(H)$ is then extracted from the χ'_{eh} and χ''_{eh} values obtained from the ω_c and Q_c data through Eqs. (3) and (6). Equations (1), (2), (9), and (10) combine to give an explicit connection relation between the effective linewidth and the susceptibility components according to

$$\Delta H_{\text{eff}} = \frac{2X_\omega \chi''_{eh}}{\omega_c X_Q \chi'_{eh}}. \tag{11}$$

In closing this section on measurement methods, it is useful to consider measurement accuracy and linewidth uncertainties. Let $U(x)$ denote the expanded uncertainty for a given measurement of x, where x can correspond to ΔH_{eff}, χ'_{eh}, χ''_{eh}, or any other relevant quantity in the measurement sequence. Note, however, that errors in X_ω, X_Q, and the factor $1/\omega_c$ can be reasonably neglected for the high field regime. Based on the standard uncertainty propagation law,[32] one can then write the relative measurement uncertainty in the effective linewidth according to

$$\frac{U(\Delta H_{\text{eff}})}{\Delta H_{\text{eff}}} = \sqrt{\left[\frac{U(\chi'_{eh})}{\chi'_{eh}}\right]^2 + \left[\frac{U(\chi''_{eh})}{\chi''_{eh}}\right]^2}. \tag{12}$$

Here, it is assumed that χ'_{eh} and χ''_{eh} correspond to the independent measurements of completely separate quantities. This is understandable since χ'_{eh} and χ''_{eh} are calculated from the separately measured Q_c and ω_c parameters and their extrapolations Q_∞ and ω_∞, respectively. Second, the errors in K are neglected because this parameter is typically obtained from the γ-optimized highly linear ω_c vs X_ω fit.

In the determinations of $U(\chi'_{eh})$ and $U(\chi'_{eh})$, one can neglect several factors. First, as just noted, one can neglect errors in K. Second, one can also neglect uncertainty contributions from the $1/\omega_c$ factor in Eq. (3) as well as the $1/(Q_c - \delta Q_c)$ and $1/Q_\infty$ factors in Eq. (6). This is because of the conditions $\omega_c \gg |\omega_c - \omega_\infty|$ and $Q_c \gg |Q_\infty - Q_c + \delta Q_c|$. As a result, one need only consider terms in $\omega_c - \omega_\infty$ and $Q_c - Q_\infty + \delta Q_c$ in the determination of $U(\Delta H_{\text{eff}})$. The final result for $U(\Delta H_{\text{eff}})$ then becomes

$$\frac{U(\Delta H_{\text{eff}})}{\Delta H_{\text{eff}}} \cong \sqrt{\left[\frac{U(\omega_c - \omega_\infty)}{\omega_c - \omega_\infty}\right]^2 + \left[\frac{U(Q_c - Q_\infty + \delta Q_c)}{Q_c - Q_\infty + \delta Q_c}\right]^2}. \tag{13}$$

Note that the $\omega_c - \omega_\infty$ and $Q_c - Q_\infty + \delta Q_c$ expressions appear in the denominators of the terms in Eq. (13). In the high field regime, these divisors become very small. This means that these parameters must be measured with an extremely high accuracy if high precision ΔH_{eff} determinations are to be achieved. The so-called *ABA* method considered in Sec. V addresses this need for high accuracy. Further considerations on uncertainty and errors will be given in Sec. V.

Sections V and VI will develop the high accuracy *ABA* approach for the $\omega_c(H)$ and $Q_c(H)$ measurements that are needed for practical effective linewidth determinations. For clarity of notation, the working values of $\omega_c(H)$ and $Q_c(H)$ that are used for the $\Delta H_{\text{eff}}(H)$ analysis will be labeled as $\omega_c^{ABA}(H)$ and $Q_c^{ABA}(H)$. The undecorated parameters ω_c and Q_c with no *ABA* superscript will be used to denote the individual field-specific measurement values for cavity frequency and Q-factor that form the basis of the *ABA* analysis.

III. MICROWAVE EFFECTIVE LINEWIDTH SPECTROMETER SYSTEM

Figure 1 shows a schematic diagram of the effective linewidth microwave spectrometer system. The system is

Downloaded 28 Nov 2007 to 129.82.140.121. Redistribution subject to AIP license or copyright; see http://rsi.aip.org/rsi/copyright.jsp

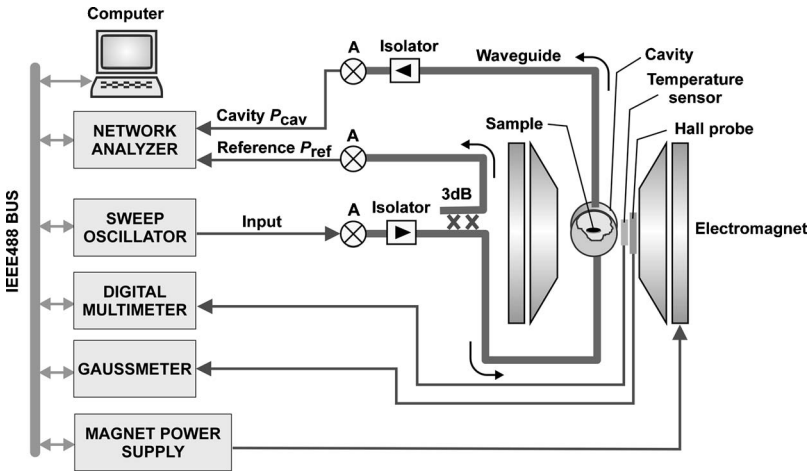

FIG. 1. Diagram of the 10 GHz effective linewidth spectrometer. The microwave system consists of a high-Q TE_{011} cylindrical cavity with a small ferrite sample mounted at the center of the cavity and input, reference, and cavity arms with waveguide to coax adaptors (A), as indicated. The instrumentation consists of a scalar network analyzer, a synthesized sweeper, a digital multimeter and temperature sensor, a Hall probe gaussmeter, and an electromagnet and power supply. All electronic components are interfaced to the control computer through a standard IEEE488 bus. The cavity is positioned in the gap of the magnet. Measurements of the microwave power levels P_{cav} and P_{ref} as a function of frequency form the basis of the overall measurement.

comprised of a synthesized sweep oscillator as a microwave source, a scalar network analyzer to measure the cavity output signal P_{cav} and reference signal P_{ref}, an electromagnet and power supply to generate the static magnetic field, a digital gaussmeter with a Hall probe for field measurement, and a digital multimeter with a temperature sensor for cavity temperature measurement.

The above elements are computer controlled through a standard IEEE488 interface. A customized Labview® program is used to manage the system, sequence the field, step the frequency, and perform specific cavity measurements. The main functions of the program are (1) to manage the microwave sweep generator and network analyzer to perform automatic cavity center frequency and quality factor measurements at fixed field and (2) to step the field between prescribed reference point and measurement point values for the measurements in (1). A software loop also manages the gaussmeter and magnet power supply to achieve precision field control. The best field stability is about ±0.003 Oe and the best field repeatability is within about 0.01 Oe.

The need for high accuracy measurements of both $\omega_c - \omega_\infty$ and $Q_c - Q_\infty + \delta Q_c$ was noted above. In order to enhance the $\omega_c - \omega_\infty$ and $Q_c - Q_\infty + \delta Q_c$ responses due to the small values of χ'_{eh} and χ''_{eh} at high field, a reasonably high-Q cavity is needed. The cavity of choice for the present system is a high-Q TE_{011} cylindrical transmission cavity with a nominal frequency of 10 GHz and a nominal quality factor of 22 000. The cavity material is oxygen-free high quality copper. The cavity itself is 3.81 cm in height and 1.99 cm in diameter. In order to achieve the highest sensitivity, the sample of interest is normally mounted at the maximal microwave field point at the center of the cavity. Typical samples for measurement can be in the form of spheres, disks, and thin films. The sample used for the demonstration measurements shown below was a 3 mm diam, 0.5 mm thick disk of ultra dense hot isostatic pressed polycrystalline yttrium iron garnet.

One obtains the cavity center frequency and quality factor from the cavity P_{cav}/P_{ref} versus frequency ω response. This response is generally comprised of about four hundred sampling points collected through the network analyzer. For optimal accuracy, the frequency point at the peak of the transmission response should always be adjusted to reside close to the center of swept frequency range. The $P_{cav}(\omega)/P_{ref}(\omega)$ response generally matches closely to a Lorentzian function. A Lorentzian best fit to the data then gives the cavity center frequency ω_c and the 3 dB width, $\Delta\omega_{3\ dB} = \omega_c/Q_c$, of the cavity resonance. The Q_c is then calculated from these two values.

Three things are important for optimal fits and accurate determinations of ω_c and Q_c. First, the optimal frequency sweep range for good fits is about 1.5 times the nominal 3 dB frequency width of the cavity transmission peak. A narrower sweep range will serve to reduce the range of values for the transmitted power and, due to the fixed power resolution of the microwave detector, will degrade accuracy. A wider sweep range also degrades the fitting accuracy because the expanded wideband cavity transmission curve corresponds to a microwave multi-interference response that is not Lorentzian. The nominal 3 dB frequency linewidth for the current cavity is about 0.5 MHz. Thus, the corresponding optimal frequency sweep interval is approximately 0.75 MHz.

Second, it is important to use the cavity transmission factor P_{cav}/P_{ref} versus ω rather than $P_{cav}(\omega)$ alone for the data fitting. In previous work, the direct cavity output power was used for the data fitting. This previous procedure is problematic because variations in the input power as well as reflections associated with small mismatches in the various microwave components can cause deviations in $P_{cav}(\omega)$ from a Lorentzian response. The distortions induced by these factors will not only change with time but can also change as the static field changes. This is because the swept frequency range must generally be shifted somewhat as H is changed, due to the change in the cavity center frequency with field. The ratio measurement eliminates most of these problems.

Third, one should also be careful in measuring each P_{cav}/P_{ref} vs ω response profile in a single sweep mode, without averaging. This is because the Lorentzian cavity response is a nonlinear curve and the average of several Lorentzian curves with different center frequencies and 3 dB widths yields a curve that is not Lorentzian. A forced fit of such an averaged response to a Lorentzian will introduce extra systematic errors in the fitted ω_c and Q_c parameters at a given field.

Downloaded 28 Nov 2007 to 129.82.140.121. Redistribution subject to AIP license or copyright; see http://rsi.aip.org/rsi/copyright.jsp

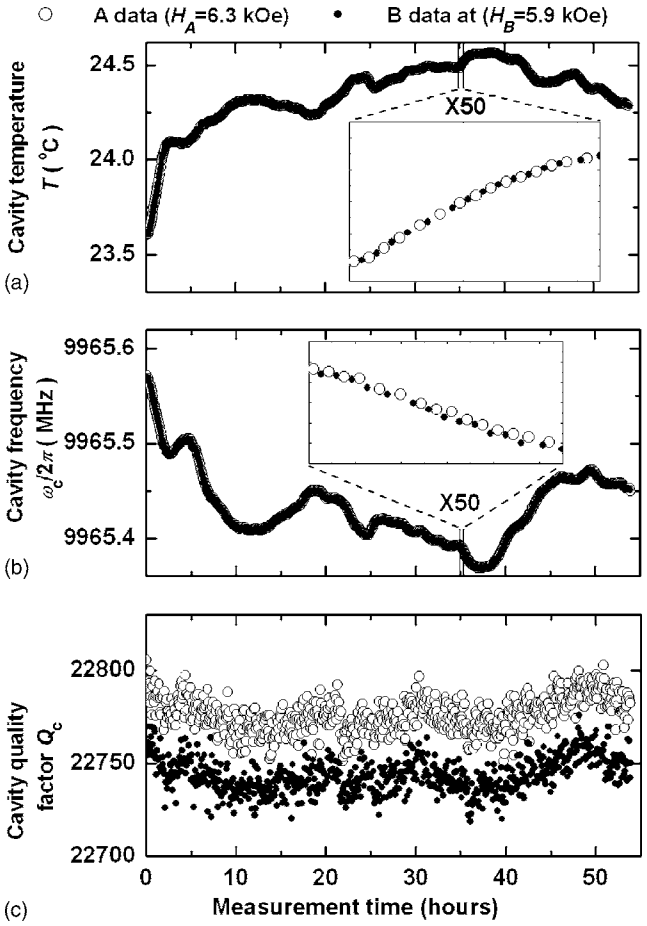

FIG. 2. Representative plots of long time *A*-*B*-*A* sequences of temperature, cavity frequency, and cavity-Q measurements for the high-Q cylindrical TE_{011} transmission cavity with an ultradense yttrium iron garnet disk at the cavity center. Graphs (a), (b), and (c) show the cavity temperature T, cavity center frequency $\omega_c/2\pi$, and quality factor Q_c vs the measurement time, respectively. The inset graphs in (a) and (b) show small sections of the data on a ×50 expanded scale for both axes. In all graphs, the open and filled black circles indicate the data points at an *A* reference field of 6.3 kOe field and a B measurement field of 5.9 kOe, respectively.

IV. CAVITY MEASUREMENTS, RANDOM ERROR, AND DRIFT

Section II presented the working equations that connect the microwave susceptibility to the ensemble of ω_c and Q_c measurement values versus field as well as those that extract the effective linewidth from the susceptibility. The section closed with brief comments on uncertainties and errors. While it is clear that high accuracy ω_c and Q_c data will yield accurate effective linewidth results, for optimum precision, it is important to isolate and quantify the dominant sources of error in the ω_c and Q_c measurements and then develop strategies to reduce these errors to the lowest possible level. This, in turn, yields final effective linewidth determinations with an extremely low uncertainty.

Figure 2 shows several sets of data from an extended test run with the measurement system described above. As already indicated, the high-Q cylindrical cavity was operated in a TE_{011} mode with a nominal center frequency at 10 GHz and with a 3 mm diam, 0.5 mm thick YIG disk mounted at cavity center. The static external field was perpendicular to the microwave magnetic field, with both fields in the plane of disk. The temperature sensor was mounted on the outside of the cavity for the recording of the cavity temperature (T). Note that the cavity was not enclosed in any sort of thermal isolation container and no measures were taken to stabilize the cavity temperature. The overall spectrometer system was allowed to warm up for about half an hour after the sample was installed. The zero reference for the time scale in Fig. 2 starts at this point.

For these demonstration measurements, two specific values of the static external field in the high field regime, namely, H_A=6.3 kOe and H_B=5.9 kOe, were programed into the control software. For convenience, the field H_A is labeled *A* and taken as the reference field, while H_B is labeled *B* and taken as the measurement field. Measurements of ω_c and Q_c were made back and forth between these *A* and *B* fields. Note that these fields are well above the fields for bulk manifold two magnon scattering. With this arrangement, it was possible to make a direct comparison of the changes in cavity parameters due to the change in field and those due to time drifts. The drifts in time are due, presumably, to the corresponding temperature drifts.

In all the graphs in Fig. 2, the *A* and *B* data points that correspond to the above reference and measurement field convention are indicated by the open and filled black circles, respectively. The measurement order of the cavity parameters is always according to the sequence *A*-*B*-*A*-*B*-*A*···. The static magnetic field at each point is extremely well stabilized, to within about ±0.05 Oe. Such small field variations at a given *A* or *B* field set point will make essentially no contribution to the changes in the cavity parameters for a given sequence of *A* or *B* set points. The use of the *A*-*B*-*A* measurement sequence, termed "the *ABA* method" in metrology jargon, then allows one to separate the variations due to field switching and time/temperature drifts. At each field set point, the ω_c and Q_c values for the cavity as well as the applicable T and H values were measured simultaneously. The data on T, ω_c, and Q_c as a function of the measurement time are shown in graphs (a), (b), and (c), respectively. Each point was taken over a fixed approximately two minute time interval.

Consider the (a), (b), and (c) graphs in Fig. 2 one by one. From (a), one sees three things. First, there is an initial warm up response for about 2 h over which the temperature increases fairly rapidly and the cavity frequency drops accordingly. Second, once this initial warm up has occurred, one sees a temperature drift with both long term (many tens of hours) and short term (hours) components. Third, as shown in the inset, there is no correlation between temperature and the back and forth field switching from H_A to H_B. This indicates that the field switching does not significantly affect the ambient temperature near the cavity, in spite of the fact that the dc current in the electromagnet coils varies as the field is stepped. Overall, one sees that the cavity temperature is mainly affected by the ambient temperature fluctuations over tens of hours. The data show that the cavity temperature drifts slowly and fairly smoothly within the typical ambient range of around 1 °C per day.

The temperature profile in (a) provides a useful reference point for the variations in ω_c and Q_c in graphs (b) and (c).

Downloaded 28 Nov 2007 to 129.82.140.121. Redistribution subject to AIP license or copyright; see http://rsi.aip.org/rsi/copyright.jsp

The frequency drifts in (b) are clearly correlated with these temperature drifts. Higher temperature means an expanding cavity and a drop in cavity frequency. From the inset in (b), one can also see that the drifts in cavity frequency with time and temperature are much larger than the random errors as well as any changes due to field switching. From the inset, one can see that the random error is on the order of and perhaps a little smaller than the jumps in frequency from the *A*-*B*-*A* changes in field.

The Q_c versus time response in (c), however, tells a different story. Here, one can see an appreciable change in Q_c as a result of the *A*-*B*-*A* field switching. This change is about four times the random error. These responses are superimposed on a drift effect that is on the same order as the random error. It is also noteworthy that the Q_c drifts correlate somewhat, albeit poorly, with the T response in (a). This correlation is only short term, on a time scale of hours, in reference to (a). There are no long term correlations on a time scale of tens of hours, as found for (a) and (b).

It is clear from the data in Fig. 2 that the drifts in ω_c and Q_c are sufficient to introduce significant measurement uncertainties if no steps are taken to adjust for these changes. Especially for the high field region of interest here, for which ω_c and Q_c have weak but critical field dependences, the distortions due to the time drifts and the random errors may be so large that it is impossible to use systematic measurements versus H to obtain accurate values of Q_∞ and ω_∞ or of the needed changes in frequency or Q.

Overall, the most important result from Fig. 2 is that the systematic cavity drifts have the same trend for both the *A*- and the *B*-field data. This correlation is crucial to the method developed here to achieve high accuracy $\omega_c(H)$ and $Q_c(H)$ data based on difference measurements. The main idea is that the point-to-point *differences* in the cavity parameters between the *A* and *B* set fields can be time independent except for random errors. This provides a possibility to eliminate the systematic time drifts through an *A*-*B*-*A* measurement sequence. This new approach to the effective linewidth measurement will be developed in Sec. V. It is the key result of this paper.

In closing this section, it is useful to revisit the time sequence data in Fig. 2 in terms of the embedded temperature profiles. Figure 3 shows the *A*-field data from Fig. 2 again, but replotted to demonstrate the explicit changes in the cavity center frequency and quality factor with temperature. The straight lines show overall linear fits. If the *B* data were included, the $\omega_c/2\pi$ vs T data in (a) would look about the same. Inclusion of the *B* data in the Q_c vs T graph in (b) would yield a similar scatter plot that is simply downshifted somewhat from the trend shown for the *A* data. Refer to Fig. 2(c).

As noted in the caption, the data in the left side of the graphs for T values from 23.5 to 24 °C or so correspond to the warm up segment of the data in Fig. 2 for the first two hours or so of measurement time. From Fig. 3(a), one sees that for this warm up region, there is a gradual and more or less linear drift in the cavity frequency. Once the warm up period is over, the right half of Fig. 3(a) shows that the overall frequency drift with temperature still follows the linear trend but with an additional component that is more complicated in nature. Presumably, if the time scale of the measurements was extended for many more tens of hours, the additional data would perform even more loops and wiggles of the sort shown on the right side of Fig. 3(a) and with a similar random pattern. The loops and wiggles give a random frequency drift with temperature of about 50 kHz that are clearly much larger than the random error. It will be shown in Sec. V that the random error in $\omega_c/2\pi$ is about ±1 kHz. It is clear from these data that, even though the random error is small, there is no reasonable way to use temperature correlations to back correct the frequency data to improve accuracy.

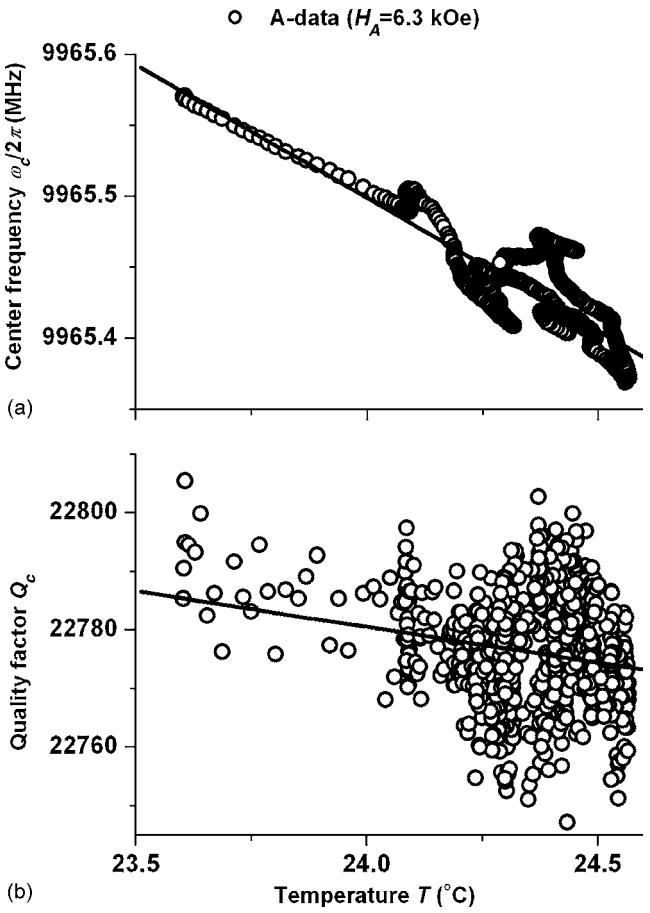

FIG. 3. Graphs (a) and (b) show plots of the cavity center frequency $\omega_c/2\pi$ and quality factor Q_c as a function of the cavity temperature. These open circle data match the *A*-field data sets from Fig. 2 for H_A=6.3 kOe. The lines show the linear fits to the overall data. Note that the data for the temperature interval from 23.5 to 24 °C correspond roughly to warm up period for the first two hours or so of measurement time in Fig. 2, while the data for 24 °C and above correspond to the remainder of the data where the drift rather than the warm up response is dominant.

What causes this temperature problem? It is likely due to temperature variations over the relatively large cavity and the complicated small but important shape changes that result. Keep in mind that the temperature is measured at only one point on the cavity exterior. The actual temperature(s) on the cavity walls will be different from this single reference point temperature. As the data show, the frequency-temperature tracking mechanism, whatever it is, is not simple. In principle, it would be necessary to map the changes in the overall

Downloaded 28 Nov 2007 to 129.82.140.121. Redistribution subject to AIP license or copyright; see http://rsi.aip.org/rsi/copyright.jsp

cavity shape with time, compute the corresponding frequency changes, and use these to back correct the data. Such an approach is not practical.

The Q_c data in Fig. 3(b) show a substantial random variation due to a combination of the complicated drifts just noted, along with the random errors present. The effective random error in the right half of the graph is about ±25 or so. The overall drift in the average Q_c is about 10/ °C as indicated by the solid line fit. One can evaluate the Q_c change for the first two hours or the temperature range from 23.6 to 24.1 °C to be about 35/ °C, more than three times the slope of the overall fit. From these drifts, along with the random response shown, it is clear that one can never achieve a high precision Q_c measurement through temperature corrections.

V. THE METROLOGICAL SUBSTITUTION *ABA* METHOD

The present solution to the problem of high accuracy measurements is found in the so-called metrological substitution *ABA* method[33,34] that has long been used in the calibration and intercomparison of metrological standards. This method provides a powerful way to eliminate the effect of the systematic, albeit complicated, drifts encountered here. This section outlines the direct application of this method to the measurement of cavity center frequency and quality factor in the context of the effective linewidth experiment.

Traditionally, the main use of the *ABA* substitution method is for the accurate measurement of small differences between two metrological standards. One can adapt the method to the present cavity measurements if the two standards are simply replaced by the quantity of interest measured at two different fields. This quantity can be the cavity frequency or quality factor. The fields are the reference field H_A that always stays the same and some measurement field H_B that may be varied. The application here is simple and straightforward. One simply chooses the *A* and *B* fields and makes a series of measurements according to the *A*-*B*-*A*-*B*-*A*-… sequence. One can then take the difference values in frequency and quality factor, repeat the measurements many times, and achieve as high accuracy as one wants from an averaging of the random errors.

Denote a given generic measurement quantity as x. A single cycle for the substitution method will consist of three x measurements, first at *A*, then at *B*, then again at *A*, and so on. In this context, one can call this approach the *ABA* method. Let the first measurement of x at the *A* field be denoted as x_{A1}. Let the second measurement of x, made after switching the field to *B*, be denoted as x_B. Then, let the third measurement of x, made after switching the field back to *A*, be denoted as x_{A2}. The ability of the *ABA* method to eliminate systematic errors depends on two conditions. First, it is important that the individual measurements be made with one fixed time interval and that the interval between measurements be as short as possible. The other condition is that the systematic drifts must be linear in time over a given *ABA* cycle. Under these conditions, the time averaged value at the *A* field can be taken as $\bar{x}_A=(x_{A1}+x_{A2})/2$ and the change in x can be taken as $\Delta x=x_B-\bar{x}_A$. Effectively, the *ABA* method amounts to simultaneous measurements at two different fields.

Are these two conditions satisfied for the cavity measurements? The answer is yes. The time interval between two neighboring points in Fig. 2 is constant, at about 2 min. An *ABA* cycle for the example shown, takes around 6 min. Given the evident temperature drift profile from Fig. 2(a), one may take the drift with time over this 6 min interval as essentially linear. One key advantage of the *ABA* method is that one does not need to take the actual drift or temperature response into account. A given parameter may be drifting up with temperature, down with temperature, or not at all. In any case, Δx should correspond to the relative change in the value of x from *A* to *B*. With all drift eliminated through this short term difference measurement, the mean value of Δx, taken here as $\overline{\Delta x}$, and the standard deviation of Δx, taken as $\sigma_{\Delta x}$, can be obtained from standard statistics for a normal distribution. More importantly, the standard deviation for the mean $\overline{\Delta x}$ is obtained as $\sigma_{\Delta x}/\sqrt{N}$, where N is the number of *ABA* cycles over which the quantity Δx is measured.

The final test, of course, is in the examination of the values of the Δx measurements from a large ensemble of individual *ABA* cycles. If, in fact, the *ABA* method has successfully eliminated all systematic errors, the remaining random errors should appear as a Gaussian distribution of the Δx values. The accuracy of the mean value will then be limited by the number of data points. For the present situation, many test data runs for both ω_c and Q_c indicate that this is indeed the case.

Figure 4 shows results from the full *ABA* analyses for the data in Fig. 2. Graph (a) shows the *ABA* temperature parameter $\Delta T_{ABA}=[T_B-(T_{A1}+T_{A2})/2]$ over a given *ABA* cycle as a function of the cycle number. Graphs (b) and (c) show the statistical distributions in $\Delta\omega_c/2\pi$ and ΔQ_c values, respectively, obtained from the 700 or so *ABA* cycles contained in the Fig. 2 data. The solid curves show Gaussian profile best fits to the respective sets of data. The correlation coefficients for the fits in (b) and (c) are 0.998 and 0.997, respectively. Recall that this particular *ABA* sequence is for a reference field $H_A=6.3$ kOe and a measurement field $H_B=5.9$ kOe.

From graph (a), one can see that the cycle-to-cycle deviations in ΔT_{ABA} are all in the millidegree range or smaller. Even more important, the shown fluctuations correspond to statistical error. Keep in mind that the overall temperature drift on the time scale of minutes, as evident from Fig. 3(a), is essentially linear with time. Graph (a) also shows slightly larger changes in ΔT_{ABA} from cycle to cycle within the first two hours of the measurement sequence. This indicates that a warm up time of several hours after sample mounting is desirable. These larger temperature changes also correlate with the nearly linear frequency shift with temperature in the left half of Fig. 3(a).

Graphs (b) and (c) show that the ensemble of data on $\Delta\omega_c$ and ΔQ_c can be fitted nicely to a standard Gaussian distribution. The good fits demonstrate the predominant random nature of these errors. The mean values of $\Delta\omega_c$ and ΔQ_c, either from the actual data averages or from the Gauss-

Downloaded 28 Nov 2007 to 129.82.140.121. Redistribution subject to AIP license or copyright; see http://rsi.aip.org/rsi/copyright.jsp

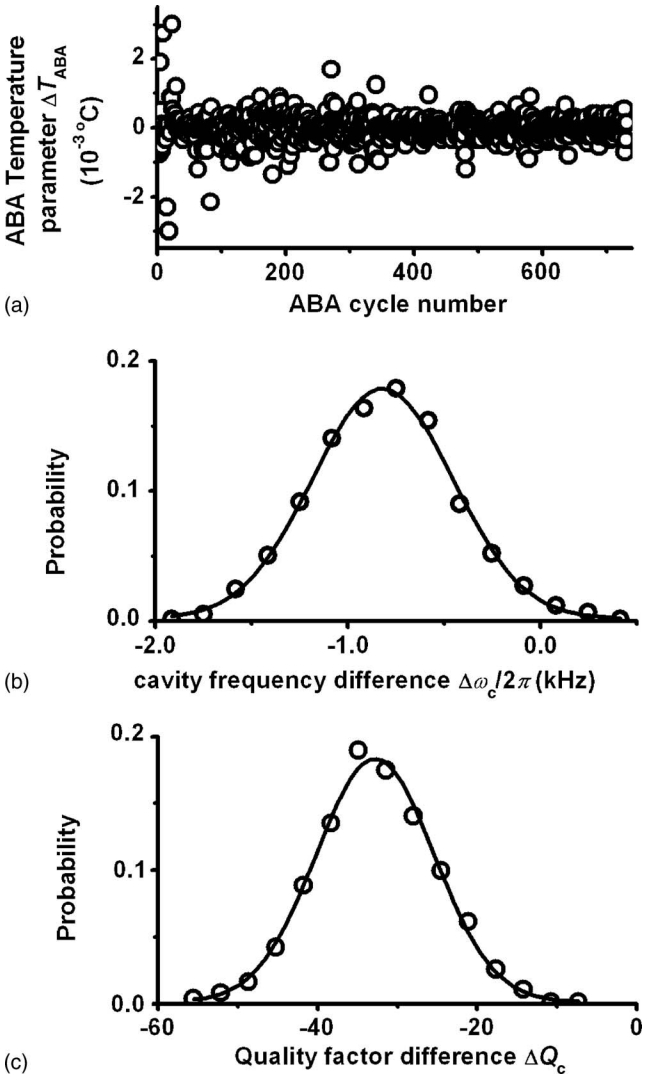

FIG. 4. Representative *ABA* analysis results based on the raw data in Fig. 2. Graph (a) shows the cavity temperature difference ΔT for a given *ABA* cycle vs the *ABA* cycle number. Graphs (b) and (c) show, respectively, the probability distributions of the corresponding $\Delta\omega_c/2\pi$ and ΔQ_c values obtained for the 700 or so *ABA* cycles of measurements displayed in Fig. 2. The solid circles show the data. The solid curves show Gaussian profile best fits to the data.

ian fits give $\overline{\Delta\omega_c}/2\pi=-0.78$ kHz and $\overline{\Delta Q_c}=-33.4$, respectively. The solid line bar symbols will be used to indicate the mean values of the indicated parameter from the ensemble of data. The profiles in Fig. 4 give the standard deviations for $\Delta\omega_c/2\pi$ and ΔQ_c at 0.36 kHz and 7.4, respectively.

The good Gaussian fits show that the *ABA* measurements of $\Delta\omega_c$ and ΔQ_c follow the well-known normal distribution for data with a random error. Keep in mind, as well, that the long time sequence of *ABA* measurements used in this example was extended for several days. This shows, rather emphatically, that the *ABA* measurement results are highly reproducible over time. This is in stark contrast with the raw ω_c and Q_c data in Figs. 2 and 3. The high level of reproducibility provides the further possibility that similar sets of measurements with the same H_A reference field and different choices of the measurement field H_B can be used to obtain highly accurate difference data for $\overline{\Delta\omega_c}(H_B)$ and $\overline{\Delta Q_c}(H_B)$.

In line with the general discussion for a generic parameter x, the fact that the errors in the $\Delta\omega_c$ and ΔQ_c measurements shown here are random and subject to statistical analysis means that the uncertainties in $\overline{\Delta\omega_c}$ and $\overline{\Delta Q_c}$ can be reduced to extremely low levels simply through the use of a sufficiently large number of *ABA* cycles. For a 95% confidence level, the corresponding expanded uncertainties are given by $U(\overline{\Delta\omega_c})=2\sigma_{\Delta\omega_c}/\sqrt{N}$ and $U(\overline{\Delta Q_c})=2\sigma_{\Delta Q_c}/\sqrt{N}$. Based on the data used above for $N=732$, one obtains $U(\overline{\Delta\omega_c})/2\pi=0.037$ kHz and $U(\overline{\Delta Q_c})=0.78$. One can see, however, that there is no need to go to such extended time *ABA* cycle measurements and large N values. For a relatively short set of *ABA* measurements with $N=25$ and a cycle of 2 h or so, the uncertainties are 0.14 kHz for frequency difference and 3 for Q difference. Such an accuracy represents an improvement over previous work by about three orders of magnitude for frequency and over an order of magnitude for quality factor.

The final point to be considered involves the connection between these high accuracy $\overline{\Delta\omega_c}$ and $\overline{\Delta Q_c}$ difference measurements and the $\omega_c^{ABA}(H)$ and $Q_c^{ABA}(H)$ data [originally $\omega_c(H)$ and $Q_c(H)$ in Sec. II] needed for the effective linewidth analysis. Based on the above, and with the generic field H in Sec. II now replaced by the measurement field H_B, one may write

$$\omega_c^{ABA}(H_B)=\overline{\omega_c}(H_A)+\overline{\Delta\omega_c}(H_B) \tag{14}$$

and

$$Q_c^{ABA}(H_B)=\overline{Q_c}(H_A)+\overline{\Delta Q_c}(H_B). \tag{15}$$

$\overline{\omega_c}(H_A)$ and $\overline{Q_c}(H_A)$ denote the average values of ω_c and Q_c from the full ensemble of measurements at the reference field H_A over the full series of measurements for all of the selected H_B values. The point to emphasize is that the effective linewidth analysis really depends only on the relative changes in the cavity frequency and quality factor with field. If one takes the same $\omega_c(H_A)$ and $Q_c(H_A)$ values for all of the measurements for different H_B values, then the operational accuracy for $\omega_c(H_B)$ and $Q_c(H_B)$ is the same as that for $\overline{\Delta\omega_c}(H_B)$ and $\overline{\Delta Q_c}(H_B)$. One does need, of course, the actual frequencies and quality factors, and not simply the difference values, for the analysis of Sec. II. Here, the reasonable choice has been made to take the add-on as the average values over the full ensemble of measurements of the cavity center frequencies and Q-factors at the reference field H_A, respectively, over all of the different H_B values.

VI. EXAMPLE HIGH FIELD EFFECTIVE LINEWIDTH RESULTS

This section provides example high field effective linewidth results based on data obtained from the approach given above. These results provide a concrete description of the full analysis procedure and demonstrate the high level of accuracy that can be achieved. The *ABA* approach, in essence, (1) allows one to use a relatively low field reference for the measurements, (2) involves no special temperature stabilization system, and (3) yields a reduction in error by an order of magnitude or more over earlier work.[27]

The sample is the same YIG disk used for the data shown in previous sections. For reference, the saturation in-

Downloaded 28 Nov 2007 to 129.82.140.121. Redistribution subject to AIP license or copyright; see http://rsi.aip.org/rsi/copyright.jsp

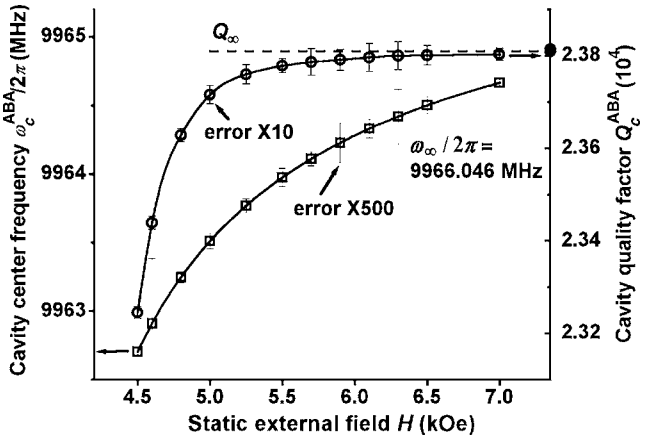

FIG. 5. Example *ABA* results on the cavity center frequency $\omega_c^{ABA}/2\pi$ and quality factor Q_c^{ABA} as a function of static external field H for the 3 mm diameter, 0.5 mm thick polycrystalline hipped YIG disk. The open circles and squares show the quality factor and cavity center frequency data, respectively. The curves through the points show the trend of the data as a guide to the eye. Error bars are expanded $\times 10$ for Q_c^{ABA} and $\times 500$ for $\omega_c^{ABA}/2\pi$, as indicated. The horizontal dashed line tied to the right side axis shows the value of the extrapolated infinite field Q parameter Q_∞. The extrapolated infinite field cavity frequency parameter ω_∞ is off the scale of the graph and has a numerical value as indicated.

duction ($4\pi M_s$) of this material is 1825 G, as measured by standard vibrating sample magnetometry for an in-plane field of 170 Oe.[35] From the classic Osborn paper,[36] the approximate in-plane and perpendicular-to-plane demagnetizing factors for disk samples can be evaluated from

$$N_\parallel = \frac{1}{2(r_d^2-1)}\left(\frac{r_d^2}{\sqrt{r_d^2-1}}\,\mathrm{asin}\,\frac{\sqrt{r_d^2-1}}{r_d}-1\right) \tag{16}$$

and

$$N_\perp = \frac{r_d^2}{r_d^2-1}\left[1-(r_d^2-1)^{-1/2}\,\mathrm{asin}\frac{\sqrt{r_d^2-1}}{r_d}\right], \tag{17}$$

respectively. Here, the r_d parameter corresponds to the disk diameter to thickness ratio. For $r_d=6$, one obtains $N_\parallel=0.11$ and $N_\perp=0.78$.

As already indicated in Secs. II and III, the disk sample is mounted at the center of the high-Q TE_{011} cylindrical cavity with the mutually perpendicular static and microwave fields in the disk plane. The cavity frequency ω_c^{ABA} and quality factor ω_c^{ABA} were measured according to the *ABA* prescription given above for 12 different values of H_B from 4.5 to 7 kOe, well above the 3.8 kOe cutoff field for degenerate magnetostatic spin wave modes at the nominal 10 GHz signal frequency. For purposes of discussion, the variable field H_B in the *ABA* measurement will generally be replaced by H. The reference field H_A was held at a fixed value of 8.0 kOe. The number of *ABA* cycles used to obtain the working set of $\Delta\omega_c$ and ΔQ_c data for each H_B (H) field ranged from 35 to 232.

Figure 5 shows data on ω_c^{ABA} and ω_c^{ABA} as a function of field. The frequency and Q_c^{ABA} data are shown by solid circles and squares, respectively. The actual frequency and Q_c^{ABA} errors are generally smaller than the size of the data points. The error bars are shown on an expanded $\times 500$ scale for frequency and $\times 10$ for quality factor. For reference, the infinite field extrapolation for the cavity Q, namely, the Q_∞ parameter introduced in previous sections, is shown by the dashed line tied to the right side axis, as indicated.

It is useful to recall the steps that lead to the realization of the ensemble of $\omega_c^{ABA}(H)$ and $Q_c^{ABA}(H)$ data and error values of the sort shown in Fig. 5. (1) For each selected measurement field ($H=H_B$), one first steps back and forth between the fixed reference field H_A and the H_B field and measures the raw cavity frequency ω_c and quality factor Q_c at each stepping field point for the desired number of *ABA* cycles. (2) One then uses the full set of difference data for $\Delta\omega_c$ and ΔQ_c to obtain the average $\overline{\Delta\omega_c}(H_B)$ and $\overline{\Delta Q_c}(H_B)$ values for the run. (3) Once all of the $\Delta\omega_c$ and ΔQ_c data have been obtained for all of the desired H_B values, one then takes the full set of individual ω_c and Q_c determinations for the H_A *field points only* and computes $\overline{\omega_c}(H_A)$ and $\overline{Q_c}(H_A)$. (4) The difference data for $\overline{\Delta\omega_c}(H_B)$ and $\overline{\Delta Q_c}(H_B)$ are then combined with the reference field values for $\overline{\omega_c}(H_A)$ and $\overline{Q_c}(H_A)$ to yield $\omega_c^{ABA}(H)$ and $Q_c^{ABA}(H)$. (5) Uncertainties are readily evaluated from the $\sigma_{\Delta\omega_c}$ and $\sigma_{\Delta Q_c}$ determinations that accompany the statistical analysis of the *ABA* data for each measurement field.

The $\omega_c^{ABA}(H)$ and $Q_c^{ABA}(H)$ data in Fig. 5 show the expected high field tail responses associated with $\chi'_{eh}(H)$ and $\chi''_{eh}(H)$, respectively. As noted in Sec. II, the quantitative extraction of the these susceptibility components and effective linewidth parameters from the data comes from the differences between these $\omega_c^{ABA}(H)$ and $Q_c^{ABA}(H)$ values and the corresponding infinite field extrapolation parameters ω_∞ and Q_∞, respectively. These ω_∞ and Q_∞ determinations are considered below. The more rapid change in $Q_c^{ABA}(H)$ and the less rapid change in $\omega_c^{ABA}(H)$ as one moves to higher fields derives from the high field limit $1/H^2$ and $1/H$ responses for $\chi''_{eh}(H)$ and $\chi'_{eh}(H)$, respectively.

One can also see from Fig. 5 that the relative frequency changes, and especially the relative quality factor changes, become quite small in the high field regime shown. Apart from their direct role in effective linewidth determinations, these small changes with field are extremely critical to the accurate determination of the K, ω_∞, and Q_∞ calibration constants. Accurate high field $\omega_c^{ABA}(H)$ and $Q_c^{ABA}(H)$ data are, therefore, especially important. Generally speaking, the small errors evident in Fig. 5 are adequate for measurements below 7 kOe or so. For higher field operation, one may need more *ABA* repetitions and the corresponding lower errors.

For these example data, the overall Q change is less than 3% and the frequency change is less than 0.02%. This implies that the cavity mode changes very little in form and the standard microwave perturbation theory provides an acceptable means for analysis as described in Sec. II. The effective linewidth extraction includes two main steps: (1) calibration constant determination and (2) evaluation of $\chi'_{eh}(H)$, $\chi''_{eh}(H)$, and $\Delta H_{\mathrm{eff}}(H)$. Step (1) is illustrated in Fig. 6. Step (2) results are shown in Fig. 7.

Graphs (a) and (b) in Fig. 6 show reduced data on ω_c^{ABA} vs X_ω and $Q_c^{ABA}-\delta Q_c$ vs X_Q. Recall that δQ_c is the eddy current loss correction from Eq. (5), with $\overline{\omega_c}(H_A)$ taken as ω_∞. The open circles show the data. The solid lines in (a) and (b) show linear and quadratic fits to the data, respectively.

Downloaded 28 Nov 2007 to 129.82.140.121. Redistribution subject to AIP license or copyright; see http://rsi.aip.org/rsi/copyright.jsp

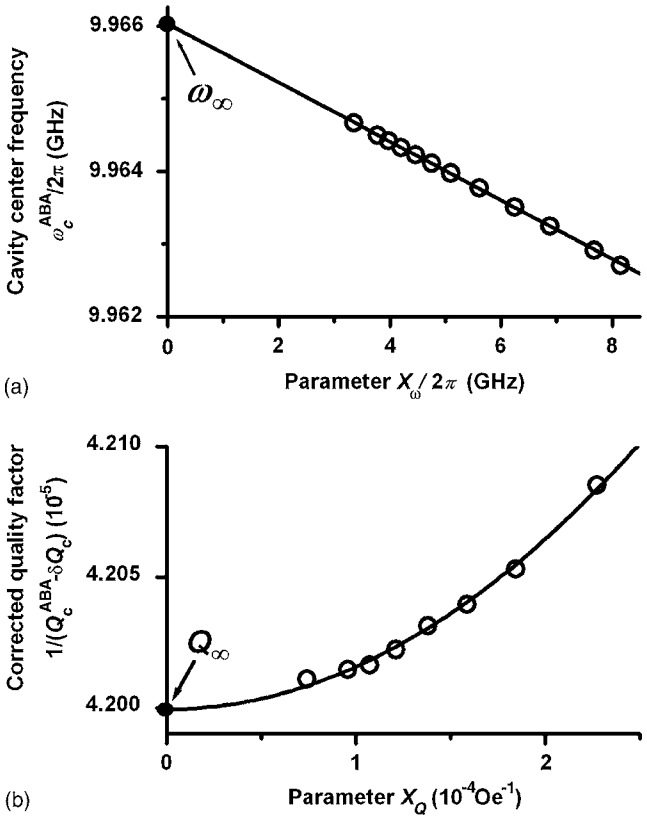

FIG. 6. Graph (a) shows the cavity resonance frequency ω_c^{ABA} as a function of the X_ω parameter from in Eq. (9). Graph (b) shows the corrected cavity quality factor Q as a function of the X_Q parameter from by Eq. (10). The open circles in both graphs show the points from the data in Fig. 5. The solid lines in (a) and (b) show linear and quadratic fits to the data, respectively. The extrapolated vertical axis intercepts of these fits at $X_\omega \to 0$ and $X_Q \to 0$ are given by the solid circle $\omega_\infty/2\pi$ and Q_∞ points, as indicated.

Keep in mind that the linear form for the (a) response follow from the perturbation theory analysis given in Sec. II. The quadratic form for the response in (b) follows from two magnon scattering considerations discussed in Ref. 24. The field ranges for graphs (a) and (b) are from 4.5 to 7 kOe and from 5 to 7 kOe, respectively. Recall that $X_\omega \to 0$ and $X_Q \to 0$ correspond to $H \to \infty$.

One can see that the line matches the data in Fig. 6(a) nearly perfectly. Keep in mind that the X_ω values for the graph (a) data display are affected by the choice of $|\gamma|$, as per the discussion of Sec. II, and that the operational value of γ is actually obtained from the optimized linear fit for $\omega_c^{ABA}(H)$ as a function of $X_\omega(H)$. Here, the optimized fit gives $|\gamma|/2\pi = 2.76$ MHz/Oe, with a correlation coefficient of 0.999 91. For a 5% change in $|\gamma|$, the fitting correlation coefficient parameter decreases to 0.999 33. The nearly perfect linear fit nicely supports the use of cavity perturbation theory for the analysis. Recall from Eq. (7), that the slope of the expected linear ω_c vs X_ω response and the $X_\omega \to 0$ intercept correspond to $-1/K$ and $\omega_\infty/2\pi$, respectively. The corresponding K and $\omega_\infty/2\pi$ values for Fig. 6(a) are 2451 and 9966.046 MHz. Perturbation theory equations with empty cavity parameters give $K_{\text{pt}} = 2615$.

One can also see that the curve and data in Fig. 6(b) also match very nicely. The correlation coefficient for the fit shown by the solid curve is 0.997 93. The δQ_c correction amounts to about a 0.01% effect. Recall that a decrease in $1/(Q_c^{ABA} - \delta Q_c)$ represents a decrease in loss. It is shown in Ref. 24 that the electromagnetic wave to spin wave (EMSW) scattering in polycrystalline YIG spheres results in a quadratic $1/(Q_c^{ABA} - \delta Q_c)$ vs X_Q high field profile. The fit in (b) shows that this same high field response also applied to disks. The fitted Q_∞ value at $X_Q \to 0$ (and $H \to \infty$) for Fig. 6(b) is 23 810.0.

Once the parameters ω_∞, Q_∞, and K are known, one can readily extract the susceptibility components $\chi'_{eh}(H)$ and $\chi''_{eh}(H)$ based on Eqs. (3) and (6) and then extract the effective linewidth from Eq. (12). Figure 7 shows final results of the analysis for ΔH_{eff} vs H. The open circles show the data. The ΔH_{eff} uncertainties are evaluated from Eq. (13). The error bars are shown in direct scale, with no multiplication factor. The solid curve shows a scaled fit based on the variation in the density of states (DOS) for the degenerate spin waves at the signal frequency with field, following the approach of Ref. 24. These results are shown here mainly for demonstration purposes. The reader should consult Ref. 24 for a full discussion of $\Delta H_{\text{eff}}(H)$ and connections to two magnon scattering, spin wave mode dispersion, and DOS considerations. Some brief comments are provided below.

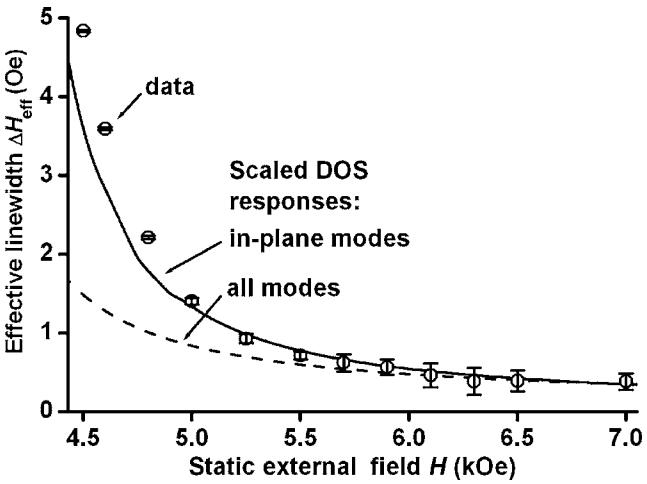

FIG. 7. High field effective linewidth vs static external field H for a 3 mm diam, 0.5 mm thick hipped YIG disk. The open circles show the data points. The curved lines show scaled density of states (DOS) curves for the degenerate electromagnetic branch spin wave modes. The solid curve is for modes with in-plane wave vectors only and the dashed curve includes all modes.

These $\Delta H_{\text{eff}}(H)$ results show the same tail response discussed at length in Ref. 24. The very small effective linewidth errors are noteworthy. They are a direct result of the meticulous use of the *ABA* method and the statistical data processing considered in detail above. The drop off in ΔH_{eff} with field is a direct result of the decrease in the DOS for degenerate electromagnetic branch spin waves.

As with the sphere results in Ref. 24, the scaled high field density of states curves in Fig. 7 matches the data reasonably well. It is interesting that for this disk sample, the DOS that includes *only* modes with in-plane wave vectors matches the data better than the DOS for all modes. This appears to be true even though the disk is quite thick and the sample is essentially a bulk sample. Similar effects have

Downloaded 28 Nov 2007 to 129.82.140.121. Redistribution subject to AIP license or copyright; see http://rsi.aip.org/rsi/copyright.jsp

been noted for critical modes at high wave number from high power measurements.[35] The slight rise in the ΔH_{eff} values at the lowest field points shown, relative to the scaled DOS curves, is likely due to a combination of two effects, an increase in the coupling and the onset of two magnon scattering for moderate wave number dipole-exchange spin waves. The two magnon effect for sphere shaped samples was discussed in Ref. 35.

The effective linewidth at the highest field for which these demonstration data were obtained, 7 kOe, is equal to 0.39 ± 0.07 Oe. This is very close to the expected 10 GHz intrinsic single crystal YIG linewidth of about 0.5 Oe. This also agrees with conclusion from Ref. 24 that the polycrystalline ferrite effective linewidth in the high field limit approaches the intrinsic linewidth found in single crystals.

The key point from Fig. 7 for this paper, however, is in the demonstration of a very high measurement accuracy. These data show that the maximum uncertainty in the high field polycrystalline sample effective linewidth is about 0.15 Oe. This is well below the intrinsic single crystal YIG linewidth. The error in previous work, as in Ref. 7, for example, generally exceeded 1 Oe. The factor of 6 or more improvement in the effective linewidth measurement uncertainty, obtained almost entirely through the use of metrology methods and modern data acquisition techniques, is remarkable. The recent results from Refs. 24 and 25 show how such precision effective linewidth measurements can lead to new physical understanding and new microwave materials analysis capabilities.

VII. SUMMARY

The above sections have described a microwave effective linewidth spectrometer system and a metrology enhanced precision effective linewidth measurement procedure. The *ABA* approach, along with computer controlled data management is demonstrated to provide a factor of 10 or more improvement in errors over previous approaches. Long time cavity tests and analysis show that the time and temperature drifts are the sources of error for the raw data on cavity center frequency and quality factor. The *ABA* metrological substitution method is adapted here to eliminate these drifts and minimize the random errors by averaging over many measurement *ABA* cycles. Sample results for a polycrystalline YIG disk demonstrate the power of the new approach.

ACKNOWLEDGMENTS

This work was supported in part by the Office of Naval Research (USA), Grant Nos. N00014-03-1-0070, N00014-06-1-0889, and N00014-07-1-0597, and the U. S. Army Research Office, Grant No. W911NF-04-1-0247.

[1] T. Kohane and E. Schlömann, J. Appl. Phys. **39**, 720 (1968).
[2] C. E. Patton, Phys. Rev. **179**, 352 (1969).
[3] E. Schlömann, Phys. Rev. **182**, 632 (1969).
[4] H. J. Van Hook and F. Euler, J. Appl. Phys. **40**, 4001 (1969).
[5] Q. H. F. Vrehen, J. Appl. Phys. **40**, 1849 (1969).
[6] E. Sawado, J. Appl. Phys. **40**, 1860 (1969).
[7] C. E. Patton, J. Appl. Phys. **41**, 1355 (1970).
[8] M. Sparks, Phys. Rev. B **1**, 3856 (1970).
[9] E. Sawado, Phys. Rev. B **14**, 000174 (1976).
[10] P. K. Singh, S. Prasad, P. K. Singh, and S. B. Singh, J. Appl. Phys. **53**, 9180 (1982).
[11] P. Kabos, T. Kato, T. Mizoguchi, and C. E. Patton, IEEE Trans. Magn. **20**, 1259 (1984).
[12] P. K. Singh, P. K. Singh, and S. Prasad, J. Phys. C **18**, 2305 (1985).
[13] M. V. Kogekar and C. E. Patton, J. Magn. Magn. Mater. **54–57**, 1139 (1986).
[14] G. A. Naziripour, C. E. Patton, and M. V. Kogekar, J. Appl. Phys. **63**, 3771 (1988).
[15] W. D. Wilber and L. M. Silber, J. Appl. Phys. **63**, 3353 (1988).
[16] K. D. McKinstry, C. E. Patton, M. A. Wittenauer, M. Sankaraman, J. Nyenhuis, F. J. Friedlaender, H. Sato, and A. Schindler, IEEE Trans. Magn. **25**, 3482 (1989).
[17] H. Moosmüller, K. D. Mckinstry, and C. E. Patton, IEEE Trans. Magn. **25**, 2482 (1990).
[18] J. R. Truedson, K. D. McKinstry, R. Karim, and C. E. Patton, IEEE Trans. Magn. **28**, 3309 (1992).
[19] J. R. Truedson, K. D. Mckinstry, and C. E. Patton, IEEE Trans. Magn. **28**, 3312 (1992).
[20] T. M. Robinson, J. Appl. Phys. **72**, 607 (1992).
[21] R. Karim, S. D. Ball, J. R. Truedson, and C. E. Patton, J. Appl. Phys. **73**, 4512 (1993).
[22] J. R. Truedson, K. D. Mckinstry, P. Kabos, and C. E. Patton, J. Appl. Phys. **74**, 2705 (1993).
[23] J. R. Truedson, P. Kabos, K. D. McKinstry, and C. E. Patton, J. Appl. Phys. **76**, 432 (1994).
[24] N. Mo, Y. Song, and C. E. Patton, J. Appl. Phys. **97**, 093901 (2005).
[25] N. Mo, J. J. Green, P. Krivosik, and C. E. Patton, J. Appl. Phys. **101**, 023914 (2007).
[26] J. J. Green and T. Kohane, Semiconductor Products and Solid State Technology **7**, 46 (1964).
[27] C. E. Patton and T. Kohane, Rev. Sci. Instrum. **43**, 76 (1972).
[28] M. A. Tsankov, S. I. Ganchev, and B. I. Vichev, J. Phys. E **18**, 708 (1985).
[29] M. Labeyrie, J. C. Mage, and J. P. Ganne, J. Appl. Phys. **64**, 5825 (1988).
[30] J. Krupka, IEEE Trans. Microwave Theory Tech. **39**, 1148 (1991).
[31] U. Hoeppe, IEEE Trans. Magn. **38**, 3126 (2002).
[32] B. N. Taylor and C. E. Kuyatt, "Guidelines for Evaluating and Expressing the Uncertainty of NIST Measurement Results," NIST Technical Note No. 1297, 1994 (unpublished).
[33] W. Bich, M. G. Cox, and P. M. Harris, Metrologia **30**, 495 (1994).
[34] C. M. Sutton and M. T. Clarkson, Metrologia **30**, 487 (1994).
[35] A. V. Nazarov, D. Ménard, J. J. Green, and C. E. Patton, J. Appl. Phys. **94**, 7227 (2003).
[36] J. A. Osborn, Phys. Rev. **67**, 351 (1945).

Downloaded 28 Nov 2007 to 129.82.140.121. Redistribution subject to AIP license or copyright; see http://rsi.aip.org/rsi/copyright.jsp